Coherence resonance in random Erdös-Rényi neural networks : mean-field theory

Axel Hutt, Thomas Wahl, Nicole Voges, Jo Hausmann, Jérémie Lefebvre

frontiers

Coherence resonance in random Erdös-Rényi neural networks : mean-field theory

A. Hutt [1,*], **T. Wahl** [1], **N. Voges** [2], **Jo Hausmann** [3], **J. Lefebvre** [4]

[1] *Team MIMESIS, INRIA Nancy Grand Est, Strasbourg, France*
[2] *ILCB & INT UMR 7289, Aix Marseille Université, Marseille, France*
[3] *R&D department, Hyland Switzerland Sarl, Geneva, Switzerland*
[4] *Krembil Research Institute, University Health Network, Toronto, Canada*

Correspondence*:
A. Hutt
axel.hutt@inria.fr

ABSTRACT

Additive noise is known to tune the stability of nonlinear systems. Using a network of two randomly connected interacting excitatory and inhibitory neural populations driven by additive noise, we derive a closed mean-field representation that captures the global network dynamics. Building on the spectral properties of Erdös-Rényi networks, mean-field dynamics are obtained via a projection of the network dynamics onto the random network's principal eigenmode. We consider Gaussian zero-mean and Poisson-like noise stimuli to excitatory neurons and show that these noise types induce coherence resonance. Specifically, the stochastic stimulation induces coherent stochastic oscillations in the γ-frequency range at intermediate noise intensity. We further show that this is valid for both global stimulation and partial stimulation, i.e. whenever a subset of excitatory neurons is stimulated only. The mean-field dynamics exposes the coherence resonance dynamics in the γ-range by a transition from a stable non-oscillatory equilibrium to an oscillatory equilibrium via a saddle-node bifurcation. We evaluate the transition between non-coherent and coherent state by various power spectra, spike-field coherence and information-theoretic measures.

Keywords: coherence resonance, phase transition, stochastic process, excitable system, mean-field, random networks

1 INTRODUCTION

Synchronisation is a well characterized phenomenon in natural systems [1]. A confluence of experimental studies indicate that synchronization may be a hallmark pattern of self-organisation [2, 3, 4]. While various mechanisms are possible, synchronization may emerge notably through an enhancement of internal interactions or via changes in external stimuli statistics. A specific type of synchronisation can occur due to random external perturbations, leading to a noise-induced coherent activity. Such a phenomenon is called coherence resonance (CR) and has been found experimentally in solid states [5], nanotubes [6] and in neural systems [7, 8]. Theoretical descriptions of CR have been developed for single excitable elements [9, 10, 9], for excitable populations [11] and for clustered networks [12].

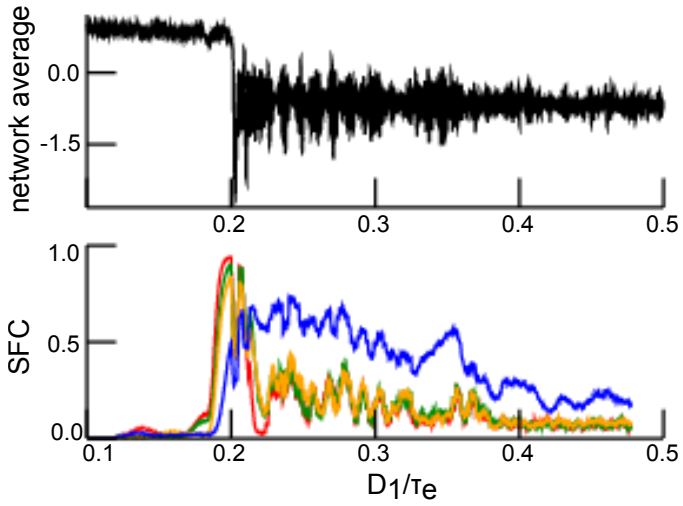

Figure 1. Synchronisation dependent on noise intensity as a marker of coherence resonance. The top panel shows the network average of $\boldsymbol{V}$ in Eq. (1) and the bottom panel provides the spike-field coherence (SFC) in the $\Theta-$(red), $\alpha-$(green), $\beta-$(orange) and $\gamma-$(blue) frequency range. For low noise intensity D_1/τ_e there is no SFC, intermediate noise intensity yields strong SFC while large noise intensities diminish SFC again. To gain the SFC values, we have integrated in time the model system with 10^4 time steps while increasing the noise variance according to (7). For illustration reasons, the SFC-values have been averaged by a sliding window of length $\Delta(D_1/\tau_e) = 0.004$. Definitions are given in section 2 and parameters are the same as in Fig. 4 with $q = 1$.

In general, stimulus-induced synchronisation is well-known in neural systems [2]. Synchronisation has been observed intracranially in the presence of noise between single neurons in specific brain areas [13, 14] and between brain areas [15, 16, 17]. The source of these random perturbations is still under debate. In this context, it is interesting to mention that [18] have found that the ascending reticular arousal system (ARAS) affects synchronisation in the visual cortex. The ARAS provides dynamic inputs to many brain areas areas [19, 20, 21]. It has thus been hypothesized that synchronisation in the visual system represents a CR effect triggered by ARAS-mediated drive. This hypothesis has been supported recently by [22] showing in numerical simulations that an intermediate intensity of noise maximises the interaction in a neural network of Hodgkin-Huxley neurons. Furthermore, recent theoretical work [21] has provided key insights on how human occipital electrocorticographic γ-activity (40-120Hz) commonly observed with open eyes [21] is closely linked to CR. Coherence resonance has further been associated with states of elevated information processing and transfer [22], which are difficult to assess in the absence of mean-field descriptions.
For illustration, Fig. 1(upper panel) shows average network activity for increasing noise intensities D_1 and one observes a jump from non-oscillatory to oscillatory activity. Moreover, the figure presents very low coherence in the network under study for weak and strong noise intensities D_1, whereas high coherence emerges for intermediate noise intensities (bottom panel). In the present work, we will explain this noise-induced coherence by a mean-field description.

To better understand the mechanisms underlying CR and its impact on information processing, we consider a simple two-population Erdös-Rényi network of interconnected McCullogh-Pitts neurons. Our goal is to use this model to provide some insight into the emergence of stimulus-induced synchronisation in neural systems and its influence on the neural network's information content. The neural network under study has random connections, a simplification inspired from the lack structure neural circuits possess at microscopic scales. Previous studies [23] have shown that such systems are capable of noise-induced

CR. Building on these results, we here provide a rigorous derivation of a mean-field equation based on an appropriate eigenmode decomposition to highlight the role of the network's connectivity - Erdös-Rényi more specifically - eigenspectrum in supporting accurate mean-field representations. We extend previous results by further considering both global (all neurons are stimulated) and partial (some neurons are stimulated) stochastic stimulation and its impact on CR similar to some previous studies [24, 25, 26]. This partial stimulation is both more general and realistic than global stimulation as considered in most previous studies [23, 11, 27]. We apply our results to both zero-mean Gaussian and Poisson-like stochastic stimuli, and derive the resulting mean-field description. It is demonstrated rigorously that partial stochastic stimulation shifts the system's dynamic topology and promotes CR, compared to global stimulation . We confirm and explore the presence of CR using various statistical measures.

2 MATERIAL AND METHODS

We first introduce the network model under study, motivate the mean-field description, mentions the nonlinear analysis employed and provides details on the statistical evaluation.

2.1 The network model

Generically, biological neuronal networks are composed of randomly connected excitatory and inhibitory neurons, which interact through synapses with opposite influence on post-synaptic cells. We assume neural populations of excitatory $\mathcal{E}$ and inhibitory $\mathcal{I}$ neurons with N neurons in each population. Excitatory neurons in $\mathcal{E}$ excite each other through the connectivity matrix $\boldsymbol{F}$, and excite inhibitory neurons in $\mathcal{I}$ through the connectivity matrix $\boldsymbol{M}$. Similarly, neurons in $\mathcal{I}$ inhibit each other by $\boldsymbol{F}$ and inhibit excitatory neurons through the connectivity matrix $\boldsymbol{M}$. Hence, $\boldsymbol{F}$ and $\boldsymbol{M}$ represent the intra-population and inter-population synaptic connections, respectively. Mathematically, such neural population interactions are described by a $2N$-dimensional non-linear dynamical system governing the evolution of the state variable vectors $\mathbf{V},\ \mathbf{W} \in \mathbb{R}^N$,

$$\begin{aligned} \tau_e \frac{d\mathbf{V}}{dt} &= -\mathbf{V} + \mathbf{F}\mathbf{S}_1[\mathbf{V}] - \mathbf{M}\mathbf{S}_2[\mathbf{W}] + \boldsymbol{e}I^e + \boldsymbol{\xi}^e(t) \\ \tau_i \frac{d\mathbf{W}}{dt} &= -\mathbf{W} + \mathbf{M}\mathbf{S}_1[\mathbf{V}] - \mathbf{F}\mathbf{S}_2[\mathbf{W}] + \boldsymbol{e}I^i + \boldsymbol{\xi}^i(t)\ . \end{aligned} \tag{1}$$

This formulation is reminiscent of many rate-based models discussed previously [28], where it is assumed that neuronal activity is asynchronous and synaptic response functions are of first order. The state variables $\mathbf{V}$ and $\mathbf{W}$ represent excitatory and inhibitory dendritic currents, respectively. The terms $\boldsymbol{\xi}^{e,i}$ represent respective stochastic inputs from various sources, such as ion channel fluctuations, stochastic input from other brain areas or external stimuli not directly accounted for in the model [29]. More specifically, we assume noise $\boldsymbol{\xi}^{e,i} \in \mathbb{R}^N$, constant input $I^{e,i}$ with $\boldsymbol{e} = (1,\dots,1)^t$. The connectivity matrices are defined by $\mathbf{F},\ \mathbf{M} \in \mathbb{R}^{N\times N}$ while the nonlinear transfer function is given by $\mathbf{S}_{1,2}[\mathbf{u}] \in \mathbb{R}^N$ with $(\mathbf{S}_1[\mathbf{u}])_n = H_0 S(u_n)$, $(\mathbf{S}_2[\mathbf{u}])_n = S(u_n)$, $H_0 > 0$ and the scalar transfer function $S(u) > 0\ \forall u \in \mathbb{R}$. Specifically, we will consider the transfer function $S(u) = \Theta(u)$ with the Heaviside function $\Theta(u) = 0\ \forall u < 0, \Theta(u) = 1\ \forall u \geq 0$. In addition, the synaptic time scales are $\tau_{e,i}$.

The present work considers directed Erdös-Rényi networks (ERN) with connection probability density $c = 0.95$, i.e. both neuron populations exhibit intra-population and inter-population non-sparse random

connections. Let us assume $\mathbf{F} = \mathbf{A}F_0$, $\mathbf{M} = \mathbf{A}M_0$ and $\mathbf{A}$ is the non-symmetric adjacency matrix of the ERN for which $(\boldsymbol{A})_{nm} = 0$ with probability $1-c$ and $(\boldsymbol{A})_{nm} = 1/cN$ with probability c. At first, let $\boldsymbol{A} = \boldsymbol{S} + \boldsymbol{U}$ with the symmetric matrix $\boldsymbol{S} = (\boldsymbol{A} + \boldsymbol{A}^t)/2$, the antisymmetric matrix $\boldsymbol{U} = (\boldsymbol{A} - \boldsymbol{A}^t)/2$ and the eigenvalues λ_A and λ_S of the matrix $\boldsymbol{A}$ and $\boldsymbol{S}$, respectively. Then $\mathcal{R}e(\lambda_A) = \lambda_S$, i.e. the real part of the eigenvalue spectrum in the directed (i.e. non-symmetric) and non-directed (i.e. symmetric) random matrix $\boldsymbol{A}$ and $\boldsymbol{S}$ is identical. Moreover, for non-directed ERNs with symmetric adjacency matrix and $N \to \infty$ its edge spectrum contains the maximum eigenvalue $\lambda_1 = 1$ with eigenvector $\boldsymbol{v}_1 = (1, 1, \ldots, 1)^t$[30, 31, 32, 33] and the bulk spectrum has the maximum eigenvalue

$$\begin{aligned} \lambda_2 &= \frac{2\sigma\sqrt{N}}{cN} \\ &= \frac{2\sqrt{1-c}}{\sqrt{cN}} \end{aligned} \tag{2}$$

with the corresponding Bernoulli distribution variance $\sigma^2 = c(1-c)$. It is obvious that $\lambda_2 \ll \lambda_1$ and $\lambda_2 \approx 0$ for large mean degree cN. Since $\mathcal{R}e(\lambda_A) = \lambda_S$, the finite-size non-symmetric connectivity matrix $\boldsymbol{F}$ ($\boldsymbol{M}$) has a maximum eigenvalue $\lambda_1 \approx F_0$ and $\lambda_{n>1} \approx 0$ ($\lambda_1 \approx M_0,\ \lambda_{n>1} \approx 0$). If c decreases, then λ_2 increases, i.e. the spectral gap decreases, and this approximation does not hold anymore. The Appendix illustrates the limits of this approximation in numerical simulations.
Figure 2(A) shows the single maximum eigenvalue λ_1 of $\boldsymbol{A}$ representing the edge spectrum and the other very small eigenvalues of the bulk spectrum. Hence, the matrix $\boldsymbol{F}$ has maximum eigenvalue F_0 and the other eigenvalues vanish. The same holds for matrix $\boldsymbol{M} = M_0\boldsymbol{A}$ with a maximum eigenvalue M_0. Figure 2(B) shows the real and imaginary part of the eigenvectors. The eigenvectors of the bulk spectrum ($i > 1$) have uniformly distributed elements in good accordance with theory of symmetric ER networks [34]. The eigenvector of the edge spectrum is $\boldsymbol{\Phi}_1 = (1, \ldots, 1)^t$, see Figure 2(C).

Moreover, we assume that each noise process at inhibitory neurons $(\boldsymbol{\eta}^i)_n = \eta_n^i$ at network node n is Gaussian distributed with zero mean, noise intensity D_2 and uncorrelated in time

$$\langle \xi_n^i(t)\xi_m^i(\tau)\rangle = 2D_2\delta_{nm}\delta(t-\tau)\ .$$

Conversely each noise process at excitatory neurons ξ_n^e belongs to a certain class $\mathcal{G}_m, m = 1, \ldots, M$ of M classes [23]. Noise processes in a specific class $\mathcal{G}_m$, i.e. $n \in \mathcal{G}_m$, share their mean $\bar{\xi}_m^e$ and variances D_1^m, i.e.

$$\langle \xi_k^e(t)\xi_l^i(\tau)\rangle = 2D_1^m\delta_{kl}\delta(t-\tau) \quad , \quad k,l \in \mathcal{G}_m\ .$$

In the following, we assume two classes $M = 2$ with $\bar{\xi}_1^e \neq 0,\ D_1^1 = D_1$ and $\bar{\xi}_2^e = 0,\ D_1^2 = 0$, i.e. only a subset of nodes $n \in \mathcal{G}_1$ are stimulated. Hence we consider a partial stimulation at number of nodes $N_1 = |\mathcal{G}_1|$.

In biological neural systems, the input to a neural population is well-described by incoming spike trains that induce dendritic currents at synaptic receptors. According to renewal theory, neurons emit spike trains whose interspike interval obeys a Poisson distribution [35]. Then incoming spike trains at mean spike rate r induce random responses at excitatory synapses with time constant τ_{in}. This random process $I_{\text{in}}(t)$ has the ensemble mean $\mathrm{E}[I_{\text{in}}] = w_{\text{in}}r\tau_{\text{in}}$ and ensemble variance $\mathrm{Var}[I_{\text{in}}] = w_{\text{in}}^2 r\tau_{\text{in}}/2$ [36] assuming the

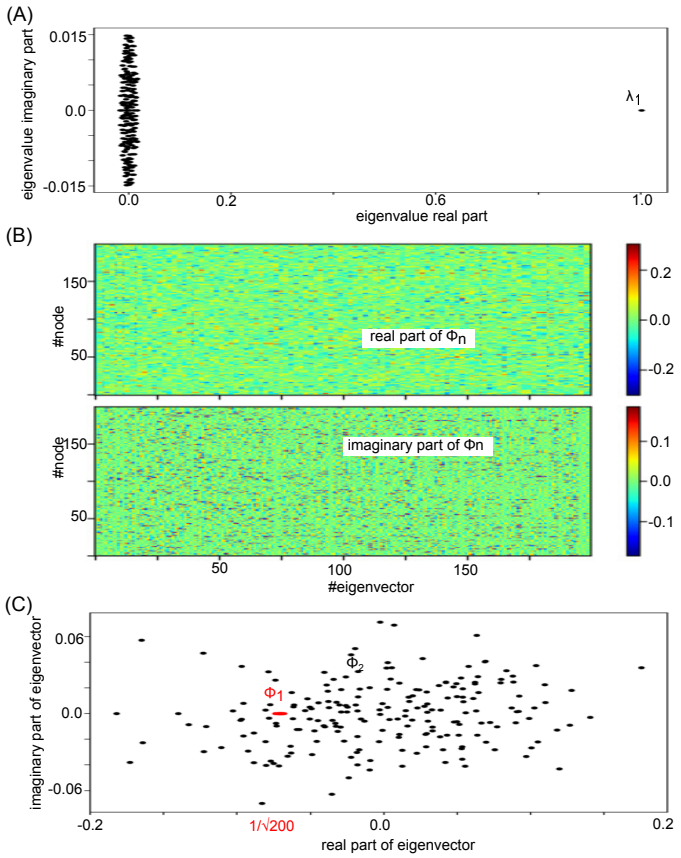

Figure 2. Eigenvalue spectrum of an Erdös-Rényi adjency matrix A under study and its eigenbasis. (A) The plot shows the eigenvalues in the complex plane demonstrating a clear spectral gap between the first eigenvalue λ_1 and the other eigenvalues $\lambda_{n>1}$. (B) The panels show the real (top) and imaginary (bottom) part of all unit-normalized eigenvectors for illustration. They appear to be random reflecting the random network topology. (C) The normalized eigenvector $\mathbf{\Phi}_1 \approx (1,\ldots,1)/\sqrt{N}$ with maximum eigenvalue $\lambda_1 \approx 1$ plotted in complex plane together with the eigenvector $\mathbf{\Phi}_2$ of the second largest eigenvalue $\lambda_2 = 0.015 + i0.0006$. Each dot corresponds to a complex-numbered vector entry in the complex plane. This result confirms the choice $\mathbf{\Phi}_1 \approx (1,\ldots,1)$ in Eqs. (9).

synaptic coupling weight $w_{\rm in}$. Since a Poisson distribution converges to a Gaussian distribution for large enough mean, we implement this input current as a Gaussian random process with mean $\mathrm{E}[I_{\rm in}]$ and variance $\mathrm{Var}[I_{\rm in}]$ while ensuring the validity of this approximation by a large enough input firing rate λ_{in}. It is important to point out that for Poisson noise, in contrast to the zero-mean Gaussian noise, both mean and variance are proportional to the input firing rate.

2.2 Conventional Mean-Field Analysis

To compare mesoscopic neural population dynamics to macroscopic experimental findings, it is commonplace to describe the network activity by the mean population response, i.e. the mean-field dynamics [37, 38, 39]. A naive mean-field approach was performed in early neuroscience studies [40, 41, 42], in which one blindly computes the mean network activity to obtain

$$\begin{aligned}\tau_e \frac{dE[V]}{dt} &= -E[V] + \mathbf{fS}_1[\mathbf{V}] - \mathbf{mS}_2[\mathbf{W}] + \boldsymbol{e}I^e \\ \tau_i \frac{dE[W]}{dt} &= -E[W] + \mathbf{mS}_1[\mathbf{V}] - \mathbf{fS}_2[\mathbf{W}] + \boldsymbol{e}I^i\end{aligned} \tag{3}$$

with the network average $E[x] = \sum_k x_k/N$ and $(\boldsymbol{f})_k = \sum_l \boldsymbol{F}_{lk}/N$, $(\boldsymbol{m})_k = \sum_l \boldsymbol{M}_{lk}/N$ assuming zero-mean external noise with $\sum_k (\boldsymbol{\xi}^{e,i})_k = 0$. In addition, one may assume identical network interactions with $(\boldsymbol{f})_k = f_0/N$ =const, $(\boldsymbol{m})_k = m_0/N$ =const and the simplifying but questionable linear assumption

$$E[S_{1,2}(x)] = S_{1,2}(E[x]) \; . \tag{4}$$

Combined, these assumptions lead to mean-field equations

$$\begin{aligned} \tau_e \frac{dE[V]}{dt} &= -E[V] + f_0 S_1[E[V]] - m_0 S_2[E[W]] \\ &\quad + \boldsymbol{e} I^e \\ \tau_i \frac{dE[W]}{dt} &= -E[W] + m_0 S_1[E[V]] - f_0 S_2[E[W]] \\ &\quad + \boldsymbol{e} I^i \end{aligned} \tag{5}$$

In this approximate description, additive noise does not affect the system dynamics.
The assumption (4) is very strong and typically not valid. In a more reasonable ansatz

$$\begin{aligned} & E\left[S_{1,2}(x)\right] \\ &= E\left[S_{1,2}(x_0) + \sum_{n=1}^{\infty} \frac{1}{n!} S_{1,2}^{(n)} (x - x_0)^n\right] \\ &= S_{1,2}(x_0) + \sum_{n=1}^{\infty} \frac{1}{n!} S_{1,2}^{(n)} E\left[(x - x_0)^n\right] \\ &= \mathcal{F}(E[x], E[x^2], E[x^3], \ldots) \end{aligned} \tag{6}$$

with $S_{1,2}^{(n)} = \partial S_{1,2}^n(x)/\partial x^n$ computed at an arbitrary point $x = x_0$ and a function $\mathcal{F}_{1,2} \in \mathbb{R}$. Hence the dynamics of the mean-field $E[V]$ depends on the higher-order statistical orders $E[V^n]$ via the nonlinear function $E\left[S_{1,2}(V)\right]$. This is called the closure problem that is solvable in specific cases only [43].

Motivated by previous studies on stochastic bifurcations [44, 45, 46, 47, 48, 49, 50, 51, 52, 53], in which additive noise may tune the stability close to the bifurcation point, the present work shows how additive noise strongly impacts the nonlinear dynamics of the system for arbitrary noise intensity and away from the bifurcation. Previous *ad-hoc* studies have already used mean-field approaches [23, 54, 55] which circumvents the closure problem (6) through a different mean-field ansatz. These motivational studies left open a more rigorous derivation. This derivation will be given in the present work: presenting in more detail its power and its limits of validity.

2.3 Equilibria, stability and quasi-cycles

The dynamic topology of a model differential equation system may be described partially by the number and characteristics of its equilibria. In general, for the non-autonomous differential equation system

$$\dot{\boldsymbol{z}} = \boldsymbol{A}\boldsymbol{z} + \boldsymbol{N}(\boldsymbol{z}) + \boldsymbol{I}(t)$$

with state variable $\boldsymbol{z} \in \mathbb{R}^N$, the driving force $\boldsymbol{I} \in \mathbb{R}^N$, the nonlinear vector $\boldsymbol{N} \in \mathbb{R}^N$ and the matrix $\boldsymbol{A} \in \mathbb{R}^{N \times N}$, it is insightful to consider the equilibria of the corresponding autonomous system $\boldsymbol{z}_0$ with

parameter	description	value
τ_e	exc. synaptic time constant	5ms
τ_i	inhib. synaptic time constant	20ms
F_0	intra-population conn. weight	2.17
M_0	inter-population conn. weight	3.87
c	connection probability	0.95
N	number of network nodes	200
I_e	constant exc. input	1.1
I_i	constant inhib. input	0.4
D_2	inhib. noise variance	0.2
w_{in}	Poisson input weight	2.1
τ_{in}	synaptic time scale of input	5ms
Δt	numerical integration step	0.5ms

Table 1. Parameter set of model (1).

$\dot{\boldsymbol{z}} = 0$ yielding the implicit condition

$$\boldsymbol{A}\boldsymbol{z}_0 = -\boldsymbol{N}(\boldsymbol{z}_0) \ .$$

The stability of an equilibrium $\boldsymbol{z}_0$ is given by the eigenvalue spectrum of the corresponding Jacobian

$$\boldsymbol{J} = \boldsymbol{A} + \boldsymbol{\nabla}\boldsymbol{N}^0$$

where $(\boldsymbol{\nabla}\boldsymbol{N}^0)_{ij} = \partial N_i(\boldsymbol{z})/\partial z_j$ computed at $\boldsymbol{z}_0$. The eigenvalues $\{\lambda_k\}$ of $\boldsymbol{J}$ can be written as $\lambda_k = a_k + i2\pi\nu_k$ with the damping a_k and the eigenfrequency ν_k. Asymptotically stable equilibria have $\Re(\lambda_k) < 0$, e.g. stable foci have $a_k < 0,\ \nu_k \in \mathbb{R}$. Linear response theory tells that noise-driven linear systems, whose deterministic dynamics exhibit a stable focus, exhibit quasi-cycles with a spectral power peak close to the eigenfrequency, see e.g. [51, 56, 57]. The smaller the noise intensity, the closer is the spectral peak frequency to the eigenfrequency. Hence, the eigenfrequency ν_k provides a reasonable estimate of the quasi-cycle spectral peak.

2.4 Numerical simulations

The Langevin equations (1) have been integrated over time utilizing the Euler-Maruyama scheme [58]. Table 1 presents the parameters used. In certain cases, the noise variance has been changed over time t according to

$$D_1(t) = D_{\min} + \frac{D_{\max} - D_{\min}}{T} t \tag{7}$$

with the maximum integration time T and the maximum and minimum noise variance values $D_{\max}$ and $D_{\min}$, respectively.

2.5 Numerical spectral data analysis

Since prominent oscillations of the network mean activity indicates synchronised activity in the population, we have computed the power spectrum of the network mean activity $\bar{V}(t) = \sum_{n=1}^{N} V_n(t)/N$ employing

the Bartlett-Welch method with overlap rate 0.8. To gain a power spectrum with frequency resolution Δf, the Bartlett-Welch segments were chosen to the length $1/\Delta f$ and the time series had a duration of 5s for the zero-mean Gaussian noise and $8s$ for the Poisson noise stimulation.

In addition to the power spectrum, the synchronisation between single neuron spike activity and the dendritic current reflects the degree of coherence in the system. To this end, we have computed the Spike Field Coherence (SFC) [59]. To estimate the SFC, we have chosen a time window of 5s for zero-mean Gaussian stimulation and 8s for Poisson stimulation and computed the spike-triggered average and power spectra in these time windows to compute the SFC for each frequency. Then we have averaged the SFC in the $\Theta-$ (4Hz-8Hz), $\alpha-$ (8Hz-12Hz), $\beta-$ (12Hz-20Hz) and $\gamma-$ (25Hz-60Hz) frequency band to gain an average SFC in the corresponding band . This standard measure estimates the coherence between spikes, that occur if $H[V_n](t) = 1$, and their corresponding dendritic currents $V_n(t)$ at the same cell averaged over all cells in the excitatory population. Significant differences of SFC at different noise intensities are evaluated by an unpaired Welch t-test with $\alpha = 0.05$.

2.6 Information measures

Coherence quantifies the degree of mutual behavior of different elements. Interestingly, recent studies of biological neural systems have shown that synchronisation and information content are related [60, 61]. For instance, under general anaesthesia asynchronous cortical activity in conscious patients is accompanied by less stored information and much available information whereas synchronous cortical activity in unconscious patients exhibits more stored information and less available information [62, 63, 19, 64, 20]. We are curious how much information is stored and available in coherence resonance described in the present work. The result may indicate a strong link between coherence and information content. To this end, we compute the amount of stored information in the excitatory population as the predictable information and the amount of available information as the population's entropy, cf. [64].

The predictable information in the excitatory population is computed as the Active Information Storage AIS [65, 66] utilizing the Gaussian Copula Mutual Information (GCMI) estimation [67]. Assuming a single time series $V_i(t)$

$$\mathrm{AIS}_i = \mathrm{MI}(V_i(t); \mathbf{V}_{\mathbf{i\Delta}}^{(\mathbf{k})}), \quad \mathbf{V}_{\mathbf{i\Delta}}^{(\mathbf{k})} = (V_i(t-\Delta), V_i(t-2\Delta), \ldots V_i(t-k\Delta)), \tag{8}$$

where MI is the mutual information [64, 68], k is the embedding dimension and Δ is the embedding delay. The value AIS_i describes how much the dendritic current $V_i(t)$ in excitatory neuron i is influenced by its past. To gain an estimate of stored information in the excitatory population, we evaluate the average stored information in the population and its variance

$$\begin{aligned} \mathrm{AIS} &= \frac{1}{N}\sum_{i=1}^{N} \mathrm{AIS}_i \\ \sigma^2_{\mathrm{AIS}} &= \frac{1}{N-1}\sum_{i=1}^{N} (\mathrm{AIS}_i - \mathrm{AIS})^2 \, . \end{aligned}$$

with $N = 200$. Significant AIS differences at different noise intensities are evaluated by an unpaired Welch t-test with $\alpha = 0.05$.

Moreover, we compute the available information in the excitatory cortex of the dendritic current $V_i(t)$ at excitatory neuron i as its entropy H_i utilizing the GCMI estimation. Its population average and variance reads

$$\begin{aligned} \mathrm{H} &= \frac{1}{N}\sum_{i=1}^{N}\mathrm{H}_i \\ \sigma_H^2 &= \frac{1}{N}\sum_{i=1}^{N}(\mathrm{H}_i-\mathrm{H})^2\,. \end{aligned}$$

and entropy differences at different noise intensities are evaluated statistically by an unpaired Welch t-test with $\alpha = 0.05$.

In subsequent sections, we have computed AIS and H for embedding dimension $k \in [1;60]$ and $\Delta \in \{\Delta t, 2\Delta t, 5\Delta t\}$ with $k\Delta = 60$ and find consistent significance test results. Specifically, we have chosen $\Delta = \Delta t$ and $k = 1$ in the shown results.

3 RESULTS

The subsequent section shows the derivation of the mean-field equations, before they are applied to describe network dynamics for two types of partial stimulation.

3.1 Mean-field description

To derive the final equations, we first introduce the idea of a mode projection before deriving the mean-field equations as a projection on the principal mode. The extension to partial stimuli extends the description.

Mode decomposition

In the model (1), the system activity $\mathbf{V} \in \mathcal{U}$ in space $\mathcal{U}$ may be expanded into a mode basis $\{\mathbf{\Phi}_n^e\},\ n = 1,\ldots,N,\ \mathbf{\Phi}_n^e \in \mathbb{C}^N$,

$$\mathbf{V} = \sum_{n=1}^{N} a_n \mathbf{\Phi}_n^e$$

with complex mode amplitude $a_n \in \mathbb{C}$ and a biorthogonal basis $\{\mathbf{\Psi}_n^e\},\ \mathbf{\Psi}_n^e \in \mathbb{C}^N$ and

$$\mathbf{\Psi}_k^{e\dagger} \mathbf{\Phi}_n^e = \delta_{kn}\ ,\ k,n = 1,\ldots,N\ .$$

Here, $\dagger$ denotes the transpose complex conjugate. The same holds for $\boldsymbol{W}$ with the basis $\{\mathbf{\Phi}_n^i\},\ n = 1,\ldots,N,\ \mathbf{\Phi}_n^i \in \mathbb{C}^N$,

$$\mathbf{W} = \sum_{n=1}^{N} b_n \mathbf{\Phi}_n^i$$

with the complex mode amplitude $b_n \in \mathbb{C}$ and the biorthogonal basis $\{\mathbf{\Psi}_n^i\},\ \mathbf{\Psi}_n^i \in \mathbb{C}^N$ and

$$\mathbf{\Psi}_k^{i\dagger} \mathbf{\Phi}_n^i = \delta_{kn}\ ,\ k,n = 1,\ldots,N\ .$$

Projecting $\mathbf{V},\ \boldsymbol{W}$ onto the respective basis $\{\mathbf{\Psi}_k^e\}$ and $\{\mathbf{\Psi}_k^i\}$, we obtain amplitude equations

$$\begin{aligned}
\tau_e \frac{da_k}{dt} &= -a_k + \mathbf{\Psi}_k^{e\dagger} \mathbf{F} \mathbf{S}_1[\mathbf{V}] - \mathbf{\Psi}_k^{e\dagger} \mathbf{M} \mathbf{S}_2[\mathbf{W}] \\
&\quad + I^e + \mathbf{\Psi}_k^{e\dagger} \boldsymbol{\xi}^e(t) \\
\tau_i \frac{db_k}{dt} &= -b_k + \mathbf{\Psi}_k^{i\dagger} \mathbf{M} \mathbf{S}_1[\mathbf{V}] - \mathbf{\Psi}_k^{i\dagger} \mathbf{F} \mathbf{S}_2[\mathbf{W}] \\
&\quad + I^i + \mathbf{\Psi}_k^{i\dagger} \boldsymbol{\xi}^i(t)\ .
\end{aligned}$$

Now let us assume that $\mathbf{\Psi}_k^e, \mathbf{\Phi}_k^e$ are eigenvectors of $\boldsymbol{F}$ with eigenvalue $\lambda_k^e \in \mathbb{C}$

$$\begin{aligned}
\mathbf{F} \mathbf{\Phi}_k^e &= \lambda_k^e \mathbf{\Phi}_k^e \\
\mathbf{\Psi}_k^{e\dagger} \mathbf{F} &= \lambda_k^e \mathbf{\Psi}_k^{e\dagger}
\end{aligned}$$

223 and $\mathbf{\Psi}_k^i, \mathbf{\Phi}_k^i$ are eigenvectors of $\boldsymbol{M}$ with eigenvalue $\lambda_k^i \mathbb{C}$

$$\begin{aligned} \mathbf{M}\mathbf{\Phi}_k^i &= \lambda_k^i \mathbf{\Phi}_k^i \\ \mathbf{\Psi}_k^{i\dagger}\mathbf{M} &= \lambda_k^i \mathbf{\Psi}_k^{i\dagger} \ . \end{aligned}$$

224 Then

$$\begin{aligned} &\lambda_1^e = F_0 \ , \ \mathbf{\Phi}_1^e = \boldsymbol{e}, \mathbf{\Psi}_1^e = \boldsymbol{e}/N \\ &\lambda_n^e \approx 0, \ n = 2, \ldots, N \ , \end{aligned} \tag{9}$$

225 cf. section 2.1, where we have utilized the bi-orthogonality of the basis. Equivalently,

$$\begin{aligned} &\lambda_1^i = M_0 \ , \ \mathbf{\Phi}_1^i = \boldsymbol{e}, \ \mathbf{\Psi}_1^i = \boldsymbol{e}/N \\ &\lambda_n^i \approx 0, \ n = 2, \ldots, N \ . \end{aligned}$$

226 We observe that $\mathbf{\Psi}_1^{i\dagger} = \mathbf{\Psi}_1^{e\dagger}$ and $\mathbf{\Phi}_1^e = \mathbf{\Phi}_1^i$.
227 The vector space $\mathcal{U}$ can be decomposed into complement subspaces $\mathcal{Z}, \ \mathcal{Z}_\perp$ with $\mathcal{U} = \mathcal{Z} \oplus \mathcal{Z}_\perp$ and
228 $\mathbf{\Psi}_1^e, \ \mathbf{\Psi}_1^i \in \mathcal{Z}$. Then $\mathbf{\Psi}_{k>1}^e, \ \mathbf{\Psi}_{k>1}^i \in \mathcal{Z}_\perp$. Each vector $\mathbf{\Psi}_{k>1}^i$ can be described in the basis $\mathbf{\Psi}_{k>1}^e$ in $\mathcal{Z}_\perp$ and
229 one gains

$$\begin{aligned} \mathbf{\Psi}_{k>1}^{i\dagger}\boldsymbol{F} &= \sum_{n=2}^{N} c_n \mathbf{\Psi}_n^{e\dagger}\boldsymbol{F} \\ &= \sum_{n=2}^{N} c_n \lambda_n^e \mathbf{\Psi}_n^{e\dagger} \\ &= 0 \end{aligned}$$

230 due to (9) and equivalently

$$\begin{aligned} \mathbf{\Psi}_{k>1}^{e\dagger}\boldsymbol{M} &= \sum_{n=2}^{N} c_n \mathbf{\Psi}_n^{i\dagger}\boldsymbol{M} \\ &= \sum_{n=2}^{N} c_n \lambda_n^i \mathbf{\Psi}_n^{i\dagger} \\ &= 0 \end{aligned}$$

with some coefficients $c_n \in \mathbb{C}$. This yields

$$\begin{aligned}
\tau_e \frac{da_1}{dt} &= -a_1 + \frac{\lambda_1^e}{N} \boldsymbol{e}^t \mathbf{S}_1[\boldsymbol{V}] - \frac{\lambda_1^i}{N} \boldsymbol{e}^t \mathbf{S}_2[\mathbf{W}] \\
&\quad + I^e + m_e(t) \qquad (10) \\
\tau_i \frac{db_1}{dt} &= -b_1 + \frac{\lambda_1^i}{N} \boldsymbol{e}^t \mathbf{S}_1[\mathbf{V}] - \frac{\lambda_1^e}{N} \boldsymbol{e}^t \mathbf{S}_2[\mathbf{W}] \\
&\quad + I^i + m_i(t) \qquad (11) \\
\tau_e \frac{da_k}{dt} &= -a_k + \boldsymbol{\Psi}_k^{e\dagger} \boldsymbol{\xi}^e(t) \ , \ k = 2, \ldots, N \qquad (12) \\
\tau_i \frac{db_k}{dt} &= -b_k + \boldsymbol{\Psi}_k^{i\dagger} \boldsymbol{\xi}^i(t) \ , \ k = 2, \ldots, N \qquad (13)
\end{aligned}$$

with $m_{e,i}(t) = \boldsymbol{e}^t \boldsymbol{\xi}^{e,i}(t)/N$.

The mean-field equations

Equations (12), (13) describe an Ornstein-Uhlenbeck process with solution

$$\begin{aligned}
a_k(t) &= \int_{-\infty}^{t} e^{-(t-\tau)/\tau_e} \boldsymbol{\Psi}_k^{e\dagger} \boldsymbol{\xi}^e(\tau) d\tau \\
b_k(t) &= \int_{-\infty}^{t} e^{-(t-\tau)/\tau_i} \boldsymbol{\Psi}_k^{i\dagger} \boldsymbol{\xi}^i(\tau) d\tau
\end{aligned} \qquad (14)$$

for $t \to \infty$. In Eqs. (10), (11) the terms $\boldsymbol{V}$, $\boldsymbol{W}$ can be written as

$$\begin{aligned}
\boldsymbol{V} &= \sum_{n=1}^{N} a_n(t) \boldsymbol{\Phi}_n^e = a_1 \boldsymbol{\Phi}_1^e + \sum_{n=2}^{N} a_n(t) \boldsymbol{\Phi}_n^e \\
\boldsymbol{W} &= \sum_{n=1}^{N} b_n(t) \boldsymbol{\Phi}_n^i = b_1 \boldsymbol{\Phi}_1^i + \sum_{n=2}^{N} b_n(t) \boldsymbol{\Phi}_n^i \ .
\end{aligned} \qquad (15)$$

Inserting expressions in Eqs. (14) into these expressions leads to

$$\begin{aligned}
\sum_{n=2}^{N} a_n(t) \boldsymbol{\Phi}_n^e &= \int_{-\infty}^{t} e^{-(t-\tau)/\tau_e} \sum_{n=2}^{N} \boldsymbol{\Phi}_n^e \boldsymbol{\Psi}_n^{e\dagger} \boldsymbol{\xi}(\tau) d\tau. \\
\sum_{n=2}^{N} b_n(t) \boldsymbol{\Phi}_n^i &= \int_{-\infty}^{t} e^{-(t-\tau)/\tau_i} \sum_{n=2}^{N} \boldsymbol{\Phi}_n^i \boldsymbol{\Psi}_n^{i\dagger} \boldsymbol{\xi}(\tau) d\tau.
\end{aligned} \qquad (16)$$

By virtue of the completeness of the basis, it is

$$\begin{aligned}
\sum_{n=2}^{N} \boldsymbol{\Phi}_n^e \boldsymbol{\Psi}_n^{e\dagger} &= \mathbf{I} - \boldsymbol{\Phi}_1^e \boldsymbol{\Psi}_1^{e\dagger} \\
\sum_{n=2}^{N} \boldsymbol{\Phi}_n^i \boldsymbol{\Psi}_n^{i\dagger} &= \mathbf{I} - \boldsymbol{\Phi}_1^i \boldsymbol{\Psi}_1^{i\dagger}
\end{aligned}$$

with the unity matrix $\mathbf{I} \in \mathbb{R}^{N\times N}$. Then inserting these identities into (16)

$$\begin{aligned}
\sum_{n=2}^{N} a_n(t)\mathbf{\Phi}_n^e &= \int_{-\infty}^{t} e^{-(t-\tau)/\tau_e}\boldsymbol{\xi}^e(\tau)d\tau \\
&\quad - \int_{-\infty}^{t} e^{-(t-\tau)/\tau_e}\mathbf{\Phi}_1^e m_e(\tau)d\tau \\
\sum_{n=2}^{N} b_n(t)\mathbf{\Phi}_n^i &= \int_{-\infty}^{t} e^{-(t-\tau)/\tau_i}\boldsymbol{\xi}^i(\tau)d\tau \\
&\quad - \int_{-\infty}^{t} e^{-(t-\tau)/\tau_i}\mathbf{\Phi}_1^i m_i(\tau)d\tau \ .
\end{aligned} \tag{17}$$

We define $\boldsymbol{\eta}^{e,i}(t) = \boldsymbol{\xi}^{e,i}(t) - \boldsymbol{\xi}_0^{e,i}$, $\boldsymbol{e}^t\boldsymbol{\eta}^{e,i}(t) = N\rho^{e,i}(t)$ with $\rho^{e,i} \sim \mathcal{N}(0, D_{1,2}/N)$ and temporally constants $\boldsymbol{\xi}_0^{e,i}$, i.e. $\rho^{e,i}$ are finite size fluctuations with variance $D_{1,2}/N$ and $\rho^{e,i} \to 0$ for $N \to \infty$. With the definitions

$$\boldsymbol{w}_{e,i}(t) = \int_{-\infty}^{t} e^{-(t-\tau)/\tau_{e,i}}\boldsymbol{\eta}^{e,i}(\tau)d\tau \tag{18}$$

$$\begin{aligned}
\boldsymbol{s}_{e,i}(t) &= \tau_e(\boldsymbol{\xi}_0^{e,i} - \boldsymbol{e}\bar{\xi_0}^{e,i}) \\
&\quad -\boldsymbol{e}\int_{-\infty}^{t} e^{-(t-\tau)/\tau_{e,i}}\rho^{e,i}(\tau)d\tau
\end{aligned} \tag{19}$$

with $\bar{\xi}_0^{e,i} = \sum_{n=1}^{N}\xi_{0,n}^{e,i}/N$ and inserting Eq. (17) into Eqs. (15)

$$\begin{aligned}
\boldsymbol{V}(t) &= a_1(t)\boldsymbol{e} + \boldsymbol{s}_e(t) + \boldsymbol{w}_e(t) \\
\boldsymbol{W}(t) &= b_1(t)\boldsymbol{e} + \boldsymbol{s}_i(t) + \boldsymbol{w}_i(t)
\end{aligned} \tag{20}$$

and the mean-field equations can the be written as

$$\begin{aligned}
\tau_e\frac{da_1}{dt} &= -a_1 + \frac{F_0}{N}\boldsymbol{e}^t\mathbf{S}_1\left[a_1(t)\boldsymbol{e} + \boldsymbol{s}_e(t) + \boldsymbol{w}_e(t)\right] \\
&\quad - \frac{M_0}{N}\boldsymbol{e}^t\mathbf{S}_2\left[b_1(t)\boldsymbol{e} + \boldsymbol{s}_i(t) + \boldsymbol{w}_i(t)\right] \\
&\quad + I^e + \bar{\xi}_0^e + \rho^e(t) \\
\tau_i\frac{db_1}{dt} &= -b_1 + \frac{M_0}{N}\boldsymbol{e}^t\mathbf{S}_1\left[a_1(t)\boldsymbol{e} + \boldsymbol{s}_e(t) + \boldsymbol{w}_e(t)\right] \\
&\quad - \frac{F_0}{N}\boldsymbol{e}^t\mathbf{S}_2\left[b_1(t)\boldsymbol{e} + \boldsymbol{s}_i(t) + \boldsymbol{w}_i(t)\right] \\
&\quad + I^i + \bar{\xi}_0^i + \rho^i(t)
\end{aligned} \tag{21}$$

By virtue of the finite-size fluctuations over time $\rho^{e,i}(t)$ the system's mean-field obeys stochastic dynamics.

Equations (14) describe an Ornstein-Uhlenbeck process of mode k and thus $\boldsymbol{w}_{e,i}(t)$ describes a multivariate Ornstein-Uhlenbeck process over time. In addition, $\boldsymbol{w}_{e,i}(t)$ is stationary over time and, since all modes k share identical properties, it is stationary over the network. Consequently, the process is ergodic and the stationary probability density function $p(w_{e,i})$ of $\boldsymbol{w}_{e,i}$ can be computed over the network yielding

$$\begin{aligned} \frac{1}{N}\boldsymbol{e}^t\mathbf{S}_1\left[x\boldsymbol{e}+\boldsymbol{w}\right] &= \frac{1}{N}\sum_{n=1}^{N} S[x+w_n] \\ &\approx \int_{-\infty}^{\infty} S(x+w)p_e(w)dw \\ &= G_1(x), \end{aligned} \tag{22}$$

where the approximation is good for large N. Specifically, for Gaussian zero-mean uncorrelated noise $\boldsymbol{\xi}_e$ with variance D [69]

$$p_e(w) = \frac{1}{\sqrt{2\pi}\sigma}e^{-w^2/2\sigma^2}\ ,\ \sigma^2 = D/\tau_e\ .$$

Similarly,

$$\begin{aligned} \frac{1}{N}\boldsymbol{e}^t\mathbf{S}_2\left[x\boldsymbol{e}+\boldsymbol{w}\right] &\approx \int_{-\infty}^{\infty} S(x+w)p_i(w)dw \\ &= G_2(x) \end{aligned} \tag{23}$$

Moreover, if the mean input is $\boldsymbol{\xi}_0^{e,i} = \alpha^{e,i}\boldsymbol{e}$ and $N\to\infty$, then $\boldsymbol{s}_{e,i} = 0$ and $\rho^{e,i} = 0$ and consequently the mean-field equation

$$\begin{aligned} \tau_e\frac{da_1}{dt} &= -a_1 + F_0G_1(a_1) - M_0G_2(b_1) + I^e + \alpha^e \\ \tau_i\frac{db_1}{dt} &= -b_1 + M_0G_1(a_1) - F_0G_2(b_1) + I^i + \alpha^i \end{aligned} \tag{24}$$

obeys deterministic dynamics. However, the above formulation depends implicitly on the additive noise through the convolution of the transfer function.

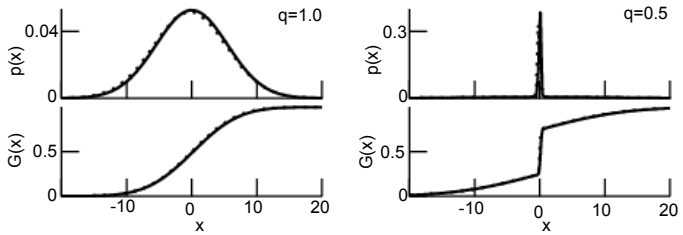

Figure 3. The probability density function p (26) and the resulting transfer function G (27). For $q = 1.0$ $D_1/\tau_e = 0.15$ and for $q = 0.5$ $D_1/\tau_e = 0.5$.

Partial stimuli

Each noise baseline stimulus at inhibitory neurons $(\boldsymbol{\xi}^i)_n = \xi_n^i$ at network node n is Gaussian distributed with zero mean and variance D_2 (cf. section 2.1). Then $\bar{\xi}_0^i = 0$, $\boldsymbol{s}_i(t) = \bar{\rho}^i(t) \sim \mathcal{N}(0, D_2/\tau_i N)$ and, considering Eq. (18), the corresponding probability density function in Eq. (23) is $p_i(w) = \mathcal{N}(0, D_2/\tau_i)$. Here $\mathcal{N}(0, \sigma^2)$ denotes a normal distribution with zero mean and variance σ^2.
Additionally, stochastic stimuli driving excitatory neurons in class $\mathcal{G}_1$ are ergodic (cf. section 2.1). Then the mean and variance of class $\mathcal{G}_1$ is

$$\begin{aligned} \bar{\xi}_1^e &= \frac{1}{N_1} \sum_{n \in \mathcal{G}_1} \xi_n^e \\ D_1 &= \frac{1}{N_1} \sum_{n \in \mathcal{G}_1} (\xi_n^e)^2 \, . \end{aligned} \tag{25}$$

Using Eq. (18) and Eq. (19) and assuming $N \to \infty$, then

$$\boldsymbol{w}^e(t) + \boldsymbol{s}^e(t) = \int_{-\infty}^{t} e^{-(t-\tau)/\tau_e} (\boldsymbol{\eta}^e(\tau) + \Delta\boldsymbol{\xi}) d\tau$$

whose probability density function $p_e(w)$ is [23]

$$\begin{aligned} p_e(w) &= \sum_{m=1}^{2} q_m \mathcal{N}(\bar{\xi}_m^e, D_1^m/\tau_e) \\ &= q\mathcal{N}(\bar{\xi}_1^e, D_1/\tau_e)[w] + (1-q)\delta(w) \end{aligned} \tag{26}$$

with $q = N_1/N$, $q_1 = q$, $q_2 = 1-q$. Here, $\Delta\boldsymbol{\xi} = (1-q, 1-q, \ldots, -q, -q)\xi_1^e$ with terms $1-q$ of number N_1 and assuming that the nodes $n = 1, \ldots, N_1$ receive stochastic input. In addition the constant input in the mean-field equation is $\bar{\xi}_0^e = q\xi_1^e$.

Then, utilizing Eqs. (22), (23) and specifying S to a step function (cf. section 2.1), the mean-field transfer functions in Eq. (24) read

$$\begin{aligned} G_1(a_1) &= \frac{H_0 q}{2} \left[1 - \mathrm{erf}\left(-\frac{a_1 - \xi_1^e}{\sqrt{2D_1/\tau_e}} \right) \right] \\ &\quad + (1-q)\Theta(a_1) \\ G_2(b_1) &= \frac{1}{2} \left[1 - \mathrm{erf}\left(-\frac{b_1}{\sqrt{2D_2/\tau_i}} \right) \right] \, . \end{aligned} \tag{27}$$

Here, $\Theta(\cdot)$ denotes the Heaviside step function. Figure 3 shows examples for p_e and G_1.

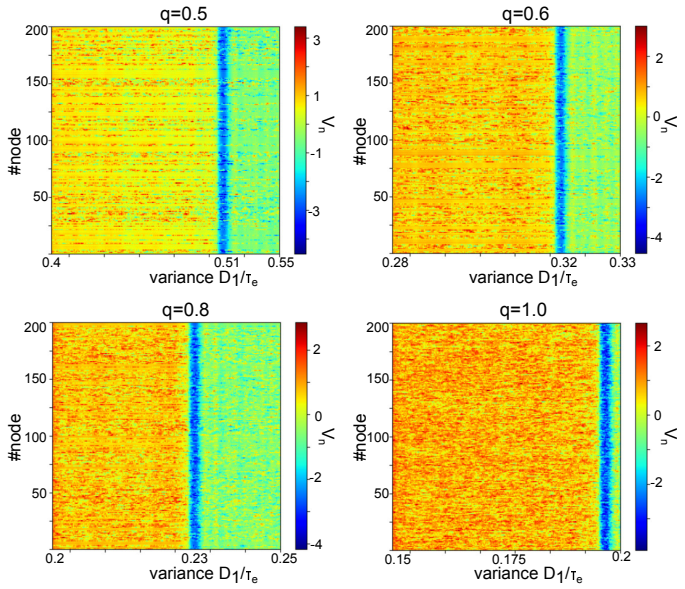

Figure 4. Enhanced zero-mean Gaussian noise induces phase transitions in spatiotemporal dynamics. The panels show the network activity $\mathbf{V(t)}$ according to Eqs. (1) with temporally increasing noise variances D_1/τ_e for different stimulus ratios q.

Essentially, the mean-field obeys

$$\begin{aligned} \tau_e \frac{da_1}{dt} &= -a_1 + F_0 G_1(a_1) - M_0 G_2(b_1) + I^e \\ &\quad + \rho^e(t) \\ \tau_i \frac{db_1}{dt} &= -b_1 + M_0 G_1(a_1) - F_0 G_2(b_1) + I^i \\ &\quad + \rho^i(t) \end{aligned} \tag{28}$$

utilizing (27).

3.2 Zero-mean Gaussian partial stimulation

At first, we consider the case of a partial noise stimulation with zero network mean, i.e. $\boldsymbol{e}^t \bar{\boldsymbol{\xi}}^e = 0$ and $\boldsymbol{s}_e(t) \sim \mathcal{N}(0, D_1/\tau_e N_1)$ and $\xi_1^e = \bar{\xi}_0^e = 0$. Then D_1 parametrizes the noise intensity only. Figure 4 shows the network evolution of $\boldsymbol{V}(t)$ for increasing noise intensities, cf. Eqs. (7). Starting from a high activity state, increasing the noise intensity yields a phase transition of the system to a network state at lower activity. This occurs for global ($q = 1.0$) and partial stimulation ($q = 0.8$, $q = 0.6$ and $q = 0.5$). Please re-call that, for instance, $q = 0.5$ reflects a stimulation where 50% of the network nodes are stimulated. These stimulated network nodes have been randomly chosen from a uniform distribution.

Figure 5 shows the respective power spectra of the network mean $\boldsymbol{V}(t)$, which provides insights about the system's synchronisation at low and high noise intensity. High noise intensity induces strong oscillations in the γ-frequency band, whereas the low noise intensity states does not - in contrast, this state shows a decaying low-pass power spectral density that is expected from a non-oscillatory stochastic process.

Stronger power spectral density at a given frequency is the signature of a coherent network, as seen in Fig. 5. Since the neurons in our network model emit spikes and exhibit synaptic input currents, noise-induced coherence may be visible in the coherence between spiking and synaptic activity as well. In fact, in Fig. 6(A) one observes a significant strongly enhanced spike-field coherence at high noise intensities for both global and partial stimulation. Hence, in sum the system exhibits coherence resonance in the sense that strong noise induces coherent oscillations that are not present at low noise intensities.

Coherence resonance is supposed to be linked to information processing in neural systems. Thus we investigate the relationship between stimulus noise intensity and information in the system across frequency bands. Figure 6(B) shows how much information is stored in the networks (AIS) and how much information is available (H). We observe that significantly more information is stored (AIS) and available (H) at high noise intensities for global stimulation $q = 1.0$, whereas high noise partial stimulation with $q = 0.8$ diminishes the stored active information and available information significantly. For more sparse stimulation with $q = 0.6$ the finding in information measures is heterogeneous and no interpretation consistent with the results for larger q is possible.

To understand this noise-induced coherence, we take a closer look at the dynamic topology of the mean-field equations (28). Their equilibria (cf. section 2.3) for negligible finite-size fluctuations $\rho^{e,i}(t) << 1$ are shown in Fig. 7 together with simulated mean-field activity $\bar{V}(t)$ for illustrative purposes. Low noise intensity induces a bistable regime with a stable node as upper equilibrium and a focus as lower equilibrium. For global stimulation ($q = 1.0$), this lower focus is unstable at very low noise intensity and stable at larger noise intensities. Moreover, the lower equilibrium is a stable focus at all noise intensities for partial ($q < 1.0$) stimulation. The center branch is always a saddle node. For larger noise intensity, the upper equilibrium branch merges with the center branch via a saddle-node bifurcation and the lower stable focus is preserved as noise is further increased. This finding remains valid for both global ($q = 1.0$) and partial ($q < 1.0$) stimulation as shown in Fig. 7 for q ranging within the interval $0.5 \leq q \leq 1.0$. One can see that for smaller q (i.e. less excitatory neurons are stimulated) the bifurcation point moves to larger noise intensities. Hence thinning out the stimulation of excitatory neurons increases the noise intensity interval at which bistability occurs. Moreover, we point out that the bifurcation points predicted by the mean-field

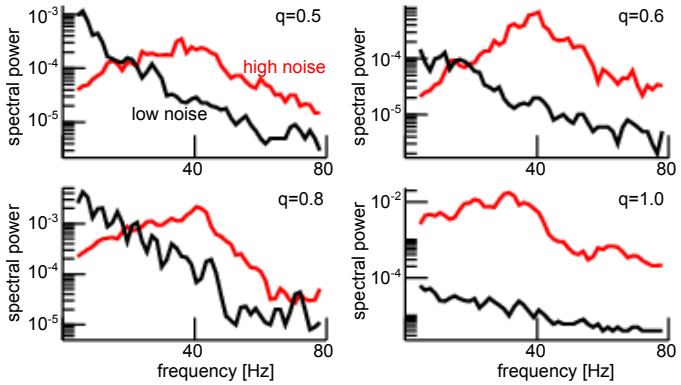

Figure 5. Enhanced noise yields strong power of the global mode $\bar{V}(t)$ in the γ-frequency range. The panels show the power spectra of $\bar{V}$ for the stimulus ratios $q = 0.5$ ($D_1/\tau_e = 0.35$ (black) and $D_1/\tau_e = 0.55$ (red)), $q = 0.6$ ($D_1/\tau_e = 0.25$ (black) and $D_1/\tau_e = 0.33$ (red)), $q = 0.8$ ($D_1/\tau_e = 0.20$ (black) and $D_1/\tau_e = 0.25$ (red)) and $q = 1.0$ ($D_1/\tau_e = 0.15$ (black) and $D_1/\tau_e = 0.20$ (red)). Power spectra at lower noise intensities are computed on the respective upper branch of the bistable system.

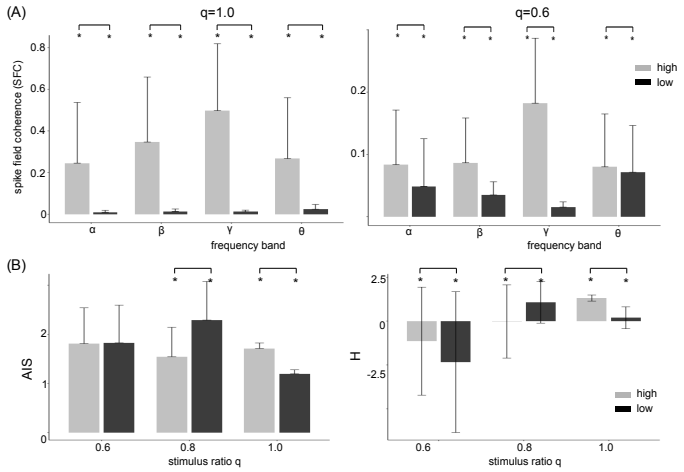

Figure 6. High zero-mean Gaussian noise enhances the Spike-Field Coherence in all frequency bands and affects heterogeneously Active Information Storage (AIS) and differential entropy (H). (A) The differences between high noise intensity (grey-colored) and low noise intensity (black-colored) is significant ($p < 0.001$) for both global and partial stimulation. (B) For global stimulation ($q = 1.0$), high noise intensity induces states of significantly enhanced stored active information (AIS) and available information (H), whereas partial stimulation with $q = 0.8$ diminishes both AIS and H significantly. Results for $q = 0.6$ are not consistent and difficult to interpret. In all panels, vertical bars denote the standard deviation, $p < 0.001$ and parameters are identical to the parameters used in Fig. 5.

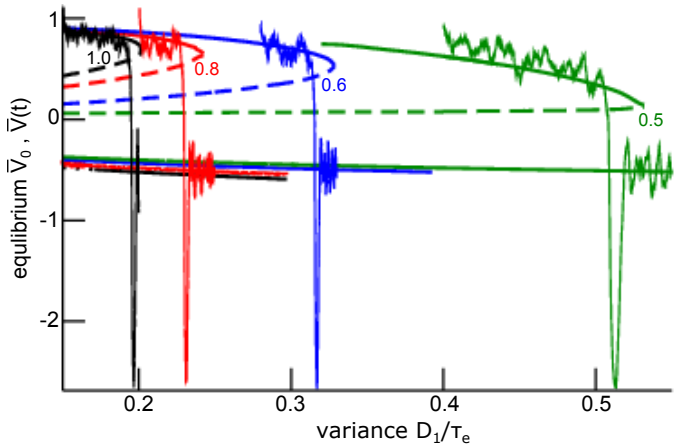

Figure 7. Equilibria and representative time series of the global mode $\bar{V}(t)$ for the zero-mean partial stimulation. There is a bistability and saddle-node bifurcation from a stable node to an stable focus at enhanced noise intensity. The numbers denote the values of the stimulus ratio q. Solid (dashed) lines mark stable (unstable) states. The time series $\bar{V}$ results from the time-varying noise intensity according to Eq. (7.)

description and shown in Fig. 7 show very good accordance to the values of D_1/τ_e in Fig. 4, where the system transitions from the upper to the lower state.

The mean-field solution involves finite-size fluctuations that affect the solutions principal oscillation frequency and magnitude. By construction, these mean-field solutions converge to the network average for increasing network size N. Figure 8 compares the time series of mean-field solutions and network averages for increasing network sizes and affirms the convergence and thus the validity of the mean-field description. It is interesting to note that, besides the mean-field dynamics, the network's dynamical properties change with increasing N as well. Figure 8 provides the principal oscillation frequencies for both solutions for

the given network size: the network speeds up with increasing size and its frequency converges to the mean-field principal frequency that remains about the same value. However, we point out that the mean-field solution remains still slightly different even for very large N since it implies the approximation of negligible connectivity matrix bulk spectra.
Figure 9 affirms this finding by comparing simulation trials of the transitions from the non-oscillatory to the oscillatory coherent state. We observe that the transition values of D_1/τ_e of the network mean and the mean-field are closer to each other for larger network size. The mean-field description (28) with (27) assumes vanishing finite-size fluctuations and these are reduced for larger network size N, i.e. the effective noise level (the finite-size fluctuations) is reduced and thus deterministic mean-field and stochastic network activity transition are closer to each other.

The frequency range of oscillations observed for steady states located within the lower branch (see Fig. 7) is a consequence of both network connectivity and neuronal properties - and is further tuned

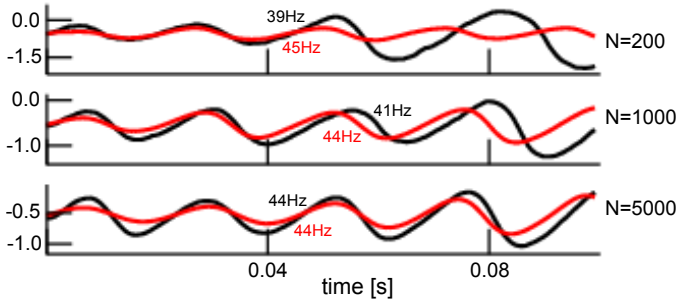

Figure 8. Comparison of network average and mean-field solution for different network sizes. The network average (black) and mean-field solutions (red) resembles more and more the larger the network of size N. This holds for the magnitude and frequency (provided in panels) of both solutions. The initial value of the mean-field activity has been chosen to the initial value of the network average. Simulations consider zero-mean Gaussian simulations with $q = 1$ and $D_1/\tau_e = 0.2$.

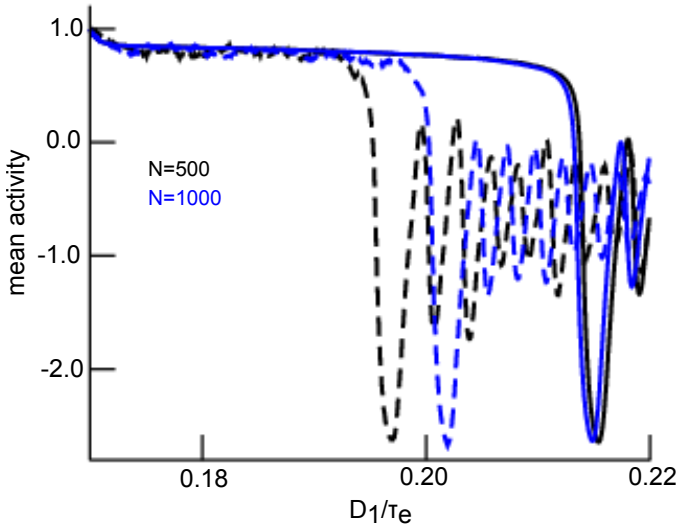

Figure 9. Comparison of transitions in network and mean-field for different network sizes. The network average (dashed line) and mean-field solutions (solid line) resemble more for larger network size N. This is explained by reduced finite-size fluctuations for larger networks. The initial value of the mean-field activity has been chosen to the initial value of the network average. Simulations consider zero-mean Gaussian simulations with $q = 1$.

by additive noise. Figure 10 shows the maximum eigenvalue real part for the upper (A) and the lower branch (B, top opanel) and the eigenfrequency (cf. subsection (2.3)) of the equilibrium at the lower branch (B, lowel panel). We observe that increasing noise intensity decreases slightly the eigenfrequency in the $\gamma-$frequency range and decreases the negative maximum eigenvalue real part. This means that additive noise increases the damping of the response of the system to perturbations - including noise. This increased noise-induced damping leads to magnitude changes in quasi-cycle solutions - which is manifested in the power spectral density distribution. Indeed, the power spectral density distribution widens as noise intensity increases, leading to the spectra as seen in Fig. 10(C). This broad spectral power distribution is the signature of suppressed coherence. As a corollary, our analysis demonstrates that coherent band-limited oscillations emerge for intermediate noise intensities only. This is a known feature of coherence resonance. For additional illustration, Fig. 1 shows the typical bell-shape of coherence (here spike-field coherence) in different frequency bands. We observe that the coherence effect is strongest in the $\gamma-$frequency range.

3.3 Poisson partial stimulation

Synaptic receptors respond to afferent Poisson-distributed input spike trains, whose properties differ substantially from the Gaussian noise processes we considered so far. To generalize our results to more physiological stimuli statistics, we considered a partial Poisson noise stimulation with dependent mean and variance. Specifically, afferent spike trains at spike rate $r_{\rm in}$ induce random responses at excitatory synapses with time constant $\tau_{\rm in}$ and synaptic weight $w_{\rm in}$. Then

$$\begin{aligned} \boldsymbol{s}^e(t) &= \tau_e \Delta \boldsymbol{\xi} + \bar{\rho}^e(t) \\ \xi_1^e &= w_{\rm in} r_{\rm in} \tau_{\rm in} \\ D_1 &= w_{\rm in} \xi_0 / 2 \\ \bar{\xi}_0^e &= q \xi_1^e \end{aligned}$$

and finite-size fluctuations $\bar{\rho}^e(t) \sim \mathcal{N}(0, D_1/N_1)$. Figure 11(A) illustrates the temporal network activity for a low and high stimuli firing rates $r_{\rm in}$. Increasing $r_{\rm in}$ induces a transition from a high-activity to a low activity state for both global and partial stimulation - similarly as in the Gaussian noise case. The high-activity state is non-oscillatory while the low-activity state is oscillatory, with frequency found in the $\gamma-$frequency range (Fig. 11(B)). In addition, the low-activity state induced by high Poisson input rate exhibits a strong spike-field coherence in contrast to the high-activity state (Fig. 11(C)). Moreover, high stimulation noise increases the stored information and the available information for global stimulation with $q = 1.0$, cf. Fig. 11(D). Information measures for partial stimulation ($q = 0.6$) are heterogeneous and an interpretation of results for AIS and H is difficult.

These results can be understood by taking a closer look at the dynamic topology of the system. Figure 12 reveals that, for global stimulation ($q = 1.0$), the system has two unstable equilibria and one stable equilibrium at lower noise intensities. The top branch is a stable node, the center branch a saddle node and the lower branch an unstable focus. There is a very small noise intensity interval at which the top and bottom branch are both stable. Increasing the Poisson stimuli firing rate leads to a sudden suppression of high-activity equilibria through a saddle-node bifurcation. Consequently, the transition observed in Fig. 11(A) is a jump from the stable node on the top bifurcation branch to the stable focus on the bottom branch similar to the effect shown in Fig. 4. For partial stimulation ($q = 0.6$), the lower branch exhibits

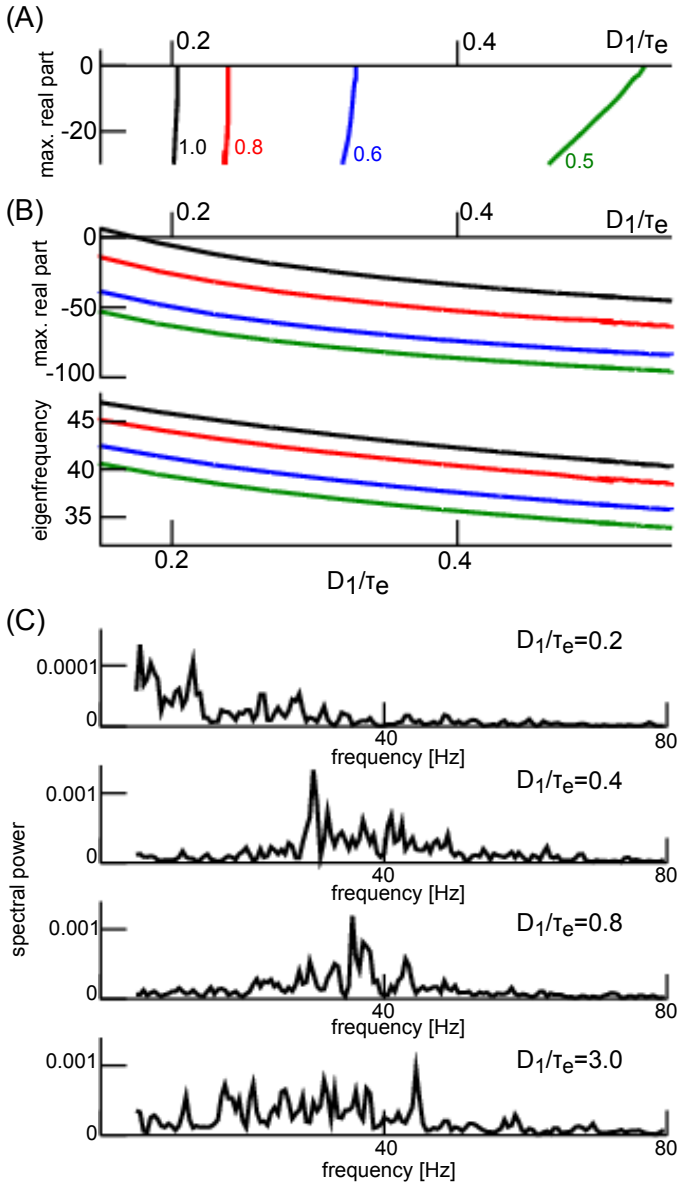

Figure 10. Eigenvalues at the top and bottom branch in Fig. 7 and corresponding power spectra. (A) maximum eigenvalue of equilibria on the top branch in Fig. 7. (B) maximum real part r of the eigenvalue $r + i2\pi\nu$ (top panel) and the corresponding eigenfrequency frequency ν. The numbers denote the values of the stimulus ratio q in all panels. (C) Power spectra of $\boldsymbol{V}(t)$ about the lower branch for $q = 0.6$ for different noise intensities D_1/τ_e.

a stable focus for much lower input firing rates. The saddle-node bifurcation is delayed, leading to an increased noise intensity interval of bistability. Hence, the system exhibits coherence resonance for Poisson noise as well.

4 DISCUSSION

This study presents a rigorous derivation of mean-field equations for two nonlinearly coupled non-sparse Erdös-Rényi networks(ERN) that are stimulated by additive noise. This mean field representation is made possible through spectral separation: the eigenspectrum of ERN networks exhibits a large spectral gap between the eigenvalue with largest real part and the rest of the spectrum. We show that the projection of the network dynamics onto the leading eigenmode represents the mean-field. Its dynamics are shaped by

eigenmodes located in the complement subspace spanned by non-leading eigenmodes. In our model, the subspace dynamics are governed and influenced by additive noise statistics and they obey an Ornstein-Uhlenbeck process.

We extended the mean-field derivation to various types of additive noise, such as global and partial noise stimuli (i.e. when only a fraction of the excitatory neurons are stimulated) and for both zero-mean Gaussian and Poisson-like noise. Collectively, our analysis shows that additive noise induces a phase transition from a non-oscillatory state to an oscillatory coherent state. Such noise-induced coherence is known as coherence resonance (CR). This phase transition has been shown to occur not only for Gaussian zero-mean noise but also for Poisson-like noise. To the best of our knowledge, CR has not been found yet for such Poisson-like noise. The general underlying mechanism is a noise-induced multiplicative impact of additive stimulation via the nonlinear coupling of different modes. This multiplicative effect modifies the net transfer function of the network and thus enlarges its dynamical repertoire. This resembles the impact of additive noise in stochastic bifurcations [51, 52, 70, 71]

Embedding into literature

Our results build on previous studies from the authors [23, 54, 55] to provide a rigorous derivation of the mean-field description, whereas previous work have motivated heuristically the mean-field reduction and, e.g., failed to show in detail whether the mean-field equation is the only solution for any given additive stimuli. Several other previous studies have presented mean-field descriptions in stochastically driven systems. For instance, Bressloff et al. [28] have derived rigorously mean-field equations for stochastic neural fields considering, inter alia, finite-element fluctuations by utilizing a Master equation and van Kampen's volume expansion approach. We note here that we also took into account finite-size fluctuations resulting from a non-negligible variance of statistical mean values. Moreover, [28] do not specify the network type and results in a rather opaque description, whereas we assume an ERN and thus exploit its unique eigenspectrum structure. This yields directly to a mean-field description, whose dependence of stochastic forces is obvious and avoids its implicit closure problem known from mean-field theories [43]. This is possible since the ERN considered share many properties with Ising models, that are known to permit an analytically treatable solution of the closure problem, see e.g. [72].

Moreover, several technical analysis steps in the present work have been applied in previous studies in a similar context. In a work on stochastic neural mean-field theory, Faugeras and colleagues [27] have assumed that the system activity fluctuations obey a normal probability distribution and have derived an effective nonlinear interaction in their Proposition 2.1 similar to our Eq. (22). Further, the authors have shown how the fluctuation correlation function, i.e. the system activity's second moment, determine the mean-field dynamics. This is in line with our result (22) showing how the mean and variance of the additive noise tunes the system's stability. However, the authors have not considered in detail the random nature of the system connectivity, whereas we have worked out the interaction of external stimulation and the ERN. This interaction yields directly the mean-field and its dependence of the external stimulus that is not present in [27]. Moreover, the present work also shows how the mean-field fluctuations affect the mean-field dynamics by deriving the fluctuation's probability density function that describes all higher moments.

Noise-induced synchronization has been found recently in a system of stochastically-driven linearly coupled FitzHugh-Nagumo neurons by Touboul and colleagues [73]. The authors have found a minimum

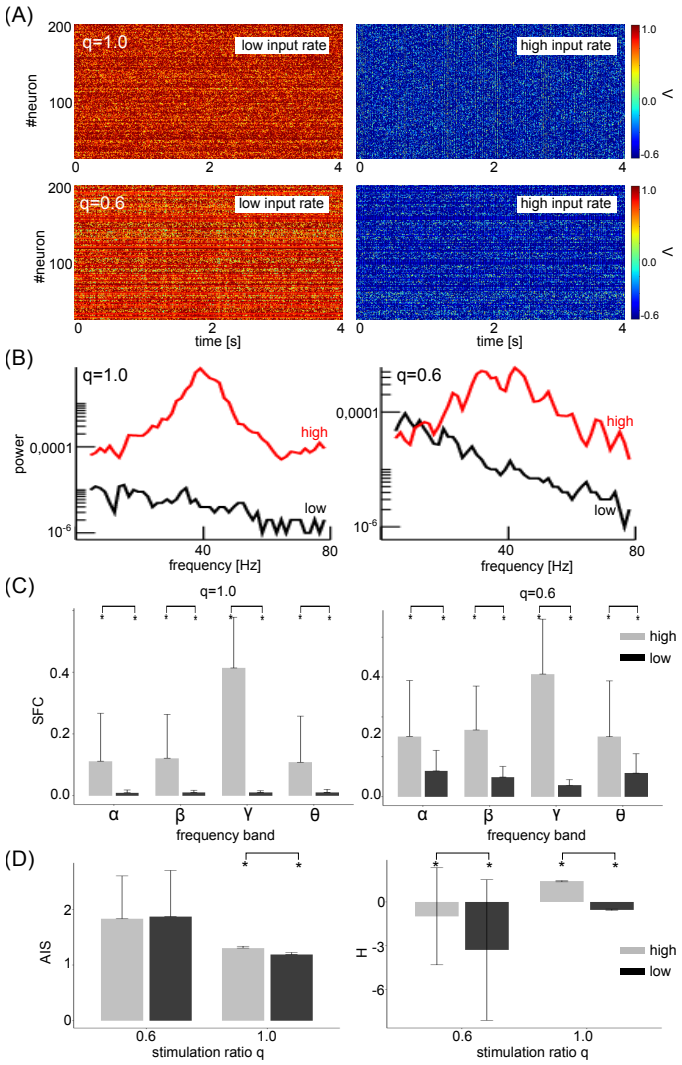

Figure 11. Poisson noise induces transitions from a non-oscillatory to an oscillatory state for both global and partial stimulation. (A) Network activity $V_n(t)$ for low input firing rate ($r = 0.04$ for $q = 1.0$ and $r = 0.09$ for $q = 0.6$) and high input firing rate ($r = 0.14$ for $q = 1.0$ and $r = 0.19$ for $q = 0.6$). For the low (high) input rate the system evolves about an upper (lower) state. (B) Power spectra of the network mean $\bar{V}(t)$ showing $\gamma-$activity for the large input rate. (C) The high input firing rate (grey-colored) induces a state of large spike-field coherence compared to the state for low input firing rate (black-colored) for both global and partial stimulation ($p < 0.01$). (D) For global stimulation ($q = 1.0$), high input firing induces a state of significantly enhanced stored active information (AIS) and available information (H). This is not consistent to results for partial stimulation ($q = 0.6$). Here is $p < 0.01$.

ratio of activated neurons that are necessary to induce global oscillatory synchronization, i.e. CR in the sense presented in our work. This question has been considered in the present work as well by asking how the mean-field dynamics, and thus how noise-induced synchronization, changes when modifying the ratio of stimulated excitatory neurons q while retaining the stimulation of inhibitory neurons. We find that global stimulation, i.e. stimulation of all excitatory neurons, yields a finite critical noise intensity below which the system is bistable and exhibits CR. Partial stimulation shifts this critical noise intensity to larger values and enlarges the bistability parameter space - and thus promotes CR.

Several previous studies of mean-field dynamics in neural systems have applied the master equation formalism [74, 75, 76]. This works nicely in completely irregular networks and the asynchronous activity

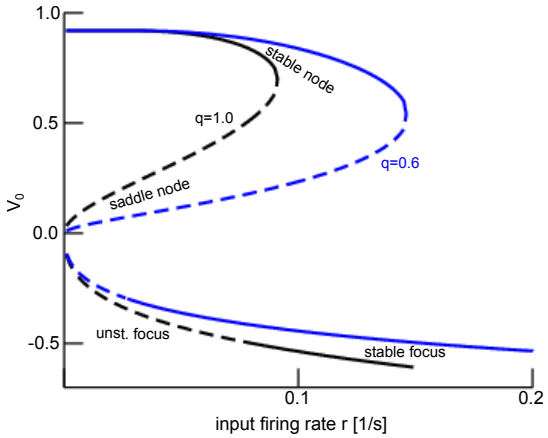

Figure 12. Equilibria of the mean-field $\bar{V}(t)$ for the Poisson partial stimulation. For global stimulation $q = 1.0$, the system is always monostable with three equilibria at low input firing rates and a single equilibrium at large input firing rates. Increasing the input firing rate from low to large firing rates, the system jumps from the upper stationary state (stable node) to a stable focus on the lower stationary state via a saddle-node bifurcation. For partial stimulation $q = 0.6$, the system is monostable with three equilibria at low input firing rates. For larger input rates, the system is bistable and passes a saddle-node bifurcation inducing a transition from a stable node to an stable focus at enhanced input firing rate r. Solid (dashed) lines mark stable (unstable) states, black- and blue-colored lines denote equilibria for global and partial stimulation, respectively. The bifurcation diagram of the mean-field $\bar{W}(t)$ is equivalent.

regime and has been applied successfully to neural populations considering biological neuron models [77, 78, 79, 80]. However, the analysis of more regular networks will be very difficult to develop with the Master equation since the implicit integration over system states would be more complex. Conversely, our presented approach may consider regular structures by a corresponding matrix eigenvalue decomposition.

At last, we mention the relation to the Master stability function [81, 82]. This function describes the stability of identical synchronisation of complex networks in a synchronisation manifold and this manifold corresponds to the mean-field in our study. Although the Master stability function has been proven to be powerful, to the best of our knowledge it does not allow to reveal coherence resonance as the current work.

Limits and outlook

The present work proposes to describe mean-field dynamics in a topological network by projection onto the networks eigenmodes. This works well for non-sparse random ERN with large connectivity probability. This network does not exhibit a spatial structure. However, less connected ERN networks show different dynamics, cf. the Appendix. Moreover, biological networks are not purely random but may exhibit distance-dependent synaptic weights [83] or spatial clusters [84]. Our specific analysis applies for networks with a large spectral gap in their eigenspectra and it might fail for biological networks with smaller spectral gaps (as shown in the Appendix). Future work will attempt to utilize the presented approach to derive mean-field dynamics for heterogeneous networks that exhibit a smaller spectral gap, such as scale-free networks [84].

Moreover, the single neuron model in the present work assumes a simple static threshold firing dynamics (McCullough-Pitts neuron) while neglecting somatic dynamics as described by Hodgkin-Huxley type models or the widely-used FitzHugh-Nagumo model [11, 73]. Future work will aim at reinforcing the

biological relevance of neurons coupled through ERN. This will be possible by extending the trivial transfer function from a step function to sigmoidal shapes for type I or type II neurons [85, 86, 76]

Our results show that noise-induced CR emerges in the $\gamma-$frequency range. This frequency band is thought to play an important role in visual information processing [13, 14, 15, 16, 17]. Experimental studies have shown that the degree of this γ-synchronization in primary cortical areas may be modulated by attention [87, 88, 59, 89]. Since attention is known to affect the ARAS activity [90] and specifically the brain stem as part of the ARAS [91] and ARAS, in turn, provides input to the cortex [92]. We conclude that it is possible that attention modulates the cortical input activity, i.e. the Poisson firing rate in our model. In this picture, attention-modulated enhanced ARAS activity induces $\gamma-$coherence and may enhance stored information [93], as shown in Figs. 6 and 11. Future more detailed brain models including the cortico-thalamic feedback and cortical interactions [57, 21] will provide further evidence whether coherence resonance is present in visual processing.

REFERENCES

[1] Pikovsky A, Rosenblum M, Kurths J. *Synchronization: A universal concept in nonlinear sciences* (Cambridge University Press) (2001).

[2] Singer W. The brain as a self-organising system. *Eur. Arch. Psychiatry Neurol. Sci.* **236** (1986) 4–9.

[3] Witthaut D, Wimberger S, Burioni R, Timme M. Classical synchronization indicates persistent entanglement in isolated quantum systems. *Nat. Commun.* **8** (2017) 14829.

[4] Hutt A, Haken H, editors. *Synergetics* (Springer-Verlag, New York) (2020).

[5] Mompo E, Ruiz-Garcia M, Carretero M, Grahn H, Zhang Y, Bonilla L. Coherence resonance and stochastic resonance in an excitable semiconductor superlattice. *Phys. Rev. Lett.* **121** (2018) 086805.

[6] Lee C, Choi W, Han JH, Strano M. Coherence resonance in a single-walled carbon nanotube ion channel. *Science* **329** (2010) 1320–1324. doi:10.1126/science.1193383.

[7] Gu H, Yang M, Li L, Liu Z, Ren W. Experimental observation of the stochastic bursting caused by coherence resonance in a neural pacemaker. *Neuroreport* **13** (2002) 1657–1660.

[8] Ratas I, Pyragas K. Noise-induced macroscopic oscillations in a network of synaptically coupled quadratic integrate-and-fire neurons. *Phys. Rev. E* **100** (2019) 052211.

[9] Pikovsky A, Kurths J. Coherence resonance in a noise-driven excitable system. *Phys. Rev. Lett.* **78** (1997) 775–778.

[10] Gang H, Ditzinger T, Ning C, Haken H. Stochastic resonance without external periodic force. *Phys. Rev. Lett.* **71** (1993) 807–810.

[11] Baspinar E, Schüler L, Olmi S, Zakharova A. Coherence resonance in neuronal populations: mean-field versus network model. *submitted* (2020).

[12] Tönjes R, Fiore C, Pereira T. Coherence resonance in influencer networks. *Nat. Commun.* **12** (2021) 72. doi:10.1038/s41467-020-20441-4.

[13] Singer W, Gray C. Visual feature integration and the temporal correlation hypothesis. *Ann. Rev. Neurosc.* **18** (1995) 555–586.

[14] Eckhorn R, Bauer R, Jordan W, Brosch M, Kruse W, Munk M, et al. Coherent oscillations: a mechanism of feature linking in the visual cortex? multiple electrode and correlation analyses in the cat. *Biol Cybern* **60** (1988) 121–130.

[15] Castelo-Branco M, Neuenschwander S, Singer W. Synchronization of visual response between the cortex, lateral geniculate nucleus, and retina in the anesthetized cat. *J. Neurosc.* **18** (1998) 6395–6410.

[16] Nelson J, Salin P, Munk M, Arzi M, Bullier J. Spatial and temporal coherence in cortico-cortical connections: a cross-correlation study in areas 17 and 18 in the cat. *Vis. Neurosci* **9** (1992) 21–37.

[17] Bressler S. Interareal synchronization in the visual cortex. *Beh. Brain Res.* **76** (1996) 37–49.

[18] Munk M, Roelfsema P, Konig P, Engel A, Singer W. Role of reticular activation in the modulation of intracortical synchronization. *Science* **272** (1996) 271–274.

[19] Hutt A, Lefebvre J, Hight D, Sleigh J. Suppression of underlying neuronal fluctuations mediates EEG slowing during general anaesthesia. *Neuroimage* **179** (2018) 414–428.

[20] Hutt A. Cortico-thalamic circuit model for bottom-up and top-down mechanisms in general anesthesia involving the reticular activating system. *Arch. Neurosci.* **6** (2019) e95498. doi:10.5812/ans.95498.

[21] Hutt A, Lefebvre J. Arousal fluctuations govern oscillatory transitions between dominant γ and α occipital activity during eyes open/closed conditions. *submitted* (2021).

[22] Pisarchik A, Maksimenko V, Andreev A, Frolov N, Makarov V, Zhuravlev M, et al. Coherent resonance in the distributed cortical network during sensory information processing. *Sci. Rep.* **9** (2019) 18325. doi:10.1038/s41598-019-54577-1.

[23] Hutt A, Lefebvre J, Hight D, Kaiser H. Phase coherence induced by additive gaussian and non-gaussian noise in excitable networks with application to burst suppression-like brain signals. *Front. Appl. Math. Stat.* **5** (2020) 69. doi:10.3389/fams.2019.00069.

[24] Chacron MJ, Longtin A, Maler L. The effects of spontaneous activity, background noise and the stimulus ensemble on information transfer in neurons. *Network Comput. Neural Syst.* **14** (2003) 803–824.

[25] Chacron MJ, Lindner B, Longtin A. Noise shaping by interval correlations increases information transfer. *Phys.Rev.Lett.* **93** (2004) 059904.

[26] Chacron MJ, doiron B, Maler L, Longtin A, Bastian J. Non-classical receptive field mediates switch in a sensory neuron's frequency tuning. *Nature* **423** (2003) 77–81. doi:10.1038/nature01590.

[27] Faugeras OD, Touboul JD, Cessac B. A constructive mean-field analysis of multi population neural networks with random synaptic weights and stochastic inputs. *Front. Comput. Neurosci.* **3** (2008) 1.

[28] Bressloff PC. Stochastic neural field theory and the system size expansion. *SIAM J. Appl. Math.* **70** (2009) 1488–1521.

[29] Terney D, Chaieb L, Moliadze V, Antal A, Paulus W. Increasing human brain excitability by Transcranial High-Frequency Random Noise Stimulation. *J. Neurosci.* **28** (2008) 14147–14155.

[30] Erdös L, Knowles A, Yau H, JYin. Spectral statistics of erdos-renyi graphs i: Local semicircle law. *Ann. Prob.* **41** (2013) 2279–2375. doi:10.1214/11-AOP734.

[31] Ding X, Jiang T. Spectral distributions of adjacency and laplacian matrices of random graphs. *Ann. Appl. Prob.* **20** (2010) 2086–2117.

[32] Kadavankandy A. *Spectral analysis of random graphs with application to clustering and sampling*. Ph.D. thesis, Université Cote d'Azur (2017). NNT : 2017AZUR4059.

[33] Füredi Z, Komlos J. The eigenvalues of random symmetric matrices. *Combinatorica* **1** (1981) 233–241.

[34] O'Rourke S, Vu V, Wang K. Eigenvectors of random matrices: A survey. *Journal of Combinatorial Theory, Series A* **144** (2016) 361–442. doi:https://doi.org/10.1016/j.jcta.2016.06.008. Fifty Years of the Journal of Combinatorial Theory.

[35] Koch C. *Biophysics of Computation* (Oxford University Press, Oxford) (1999).

[36] Ross S. *Stochastic processes (Probability and Mathemati- cal Statistics)* (Wiley) (1982).

[37] Wright J, Kydd R. The electroencephaloggram and cortical neural networks. *Network* **3** (1992) 341–362.

[38] Nunez P. Toward a quantitative description of large-scale neocortical dynamic function and EEG. *Behav. Brain Sci.* **23** (2000) 371–437.

[39] Nunez P, Srinivasan R. *Electric Fields of the Brain: The Neurophysics of EEG* (Oxford University Press, New York - Oxford) (2006).

[40] Wilson H, Cowan J. Excitatory and inhibitory interactions in localized populations of model neurons. *Biophys. J.* **12** (1972) 1–24.

[41] Gerstner W, Kistler W. *Spiking Neuron Models* (Cambridge University Press, Cambridge) (2002).

[42] Bressloff PC, Coombes S. Physics of the extended neuron. *Int. J. Mod. Phys. B* **11** (1997) 2343–2392.

[43] Kuehn C. Moment-closure - a brief review. Schöll E, Klapp S, Hövel P, editors, *Control of Self-Organizing Nonlinear Systems* (Springer, Heidelberg) (2016), 253–271. doi:10.1007/978-3-319-28028-8_13.

[44] Sri Namachchivaya N. Stochastic bifurcation. *Applied Mathematics and Computation* **39** (1990) 37s–95s. doi:https://doi.org/10.1016/0096-3003(90)90003-L.

[45] Berglund N, Gentz B. Geometric singular perturbation theory for stochastic differential equations. *J. Diff. Eq.* **191** (2003) 1–54.

[46] Bloemker D, Hairer M, Pavliotis GA. Modulation equations: Stochastic bifurcation in large domains. *Commun. Math. Phys.* **258** (2005) 479–512.

[47] Boxler P. A stochastic version of the center manifold theorem. *Prob. Th. Rel. Fields* **83** (1989) 509–545.

[48] Hutt A, Lefebvre J. Stochastic center manifold analysis in scalar nonlinear systems involving distributed delays and additive noise. *Markov Proc. Rel. Fields* **22** (2016) 555–572.

[49] Lefebvre J, Hutt A, LeBlanc V, Longtin A. Reduced dynamics for delayed systems with harmonic or stochastic forcing. *Chaos* **22** (2012) 043121.

[50] Hutt A. Additive noise may change the stability of nonlinear systems. *Europhys. Lett.* **84** (2008) 34003.

[51] Hutt A, Longtin A, Schimansky-Geier L. Additive noise-induced Turing transitions in spatial systems with application to neural fields and the Swift-Hohenberg equation. *Physica D* **237** (2008) 755–773.

[52] Hutt A, Longtin A, Schimansky-Geier L. Additive global noise delays Turing bifurcations. *Phys. Rev. Lett.* **98** (2007) 230601.

[53] Hutt A, Lefebvre J. Additive noise tunes the self-organization in complex systems. Hutt A, Haken H, editors, *Synergetics* (Springer, New York), Encyclopedia of Complexity and Systems Science Series (2020), 183.

[54] Lefebvre J, Hutt A, Knebel J, Whittingstall K, Murray M. Stimulus statistics shape oscillations in nonlinear recurrent neural networks. *J. Neurosci.* **35** (2015) 2895–2903.

[55] Hutt A, Mierau A, Lefebvre J. Dynamic control of synchronous activity in networks of spiking neurons. *PLoS One* **11** (2016) e0161488. doi:10.1371/journal.pone.0161488.

[56] Hutt A, Sutherland C, Longtin A. Driving neural oscillations with correlated spatial input and topographic feedback. *Phys.Rev.E* **78** (2008) 021911.

[57] Hashemi M, Hutt A, Sleigh J. How the cortico-thalamic feedback affects the EEG power spectrum over frontal and occipital regions during propofol-induced anaesthetic sedation. *J. Comput. Neurosci.* **39** (2015) 155.

[58] Klöden PE, Platen E. *Numerical Solution of Stochastic Differential Equations* (Springer-Verlag, Heidelberg) (1992).

[59] Fries P, Reynolds J, Rorie A, Desimone R. Modulation of oscillatory neuronal synchronization by selective visual attention. *Science* **291** (2001) 1560–1563.

[60] Tononi G. An information integration theory of consciousness. *BMC Neurosci.* **5** (2004) 42.

[61] Alkire M, Hudetz A, GTononi. Consciousness and anesthesia. *Science* **322** (2008) 876–880. doi:10.1126/science.1149213.

[62] Lee M, Sanders R, SK Yeom DW, Seo K, Kim H, Tononi G, et al. Network properties in transistions of consciousness during propofol-induced sedation. *Sci. Rep.* **7** (2017) 16791.

[63] Massimini M, Ferrarelli F, Huber R, Esser SK, Singh H, Tononi G. Breakdown of cortical effective connectivity during sleep. *Science* **309** (2005) 2228–2232.

[64] Wollstadt P, Sellers K, Rudelt L, Priesemann V, Hutt A, Frohlich F, et al. Breakdown of local information processing may underlie isoflurane anesthesia effects. *PLoS Comput. Biol.* **13** (2017) e1005511.

[65] Lizier J, Prokopenko M, Zomaya A. Local measures of information storage in complex distributed computation. *Information Science* **208** (2012) 39–54.

589 [66] Wibral M, Lizier J, Vögler S, Priesemann V, Galuske R. Local active information storage as a tool to
590 understand distributed neural information processing. *Front. Neuroinform.* **8** (2014) 1.
591 [67] Ince R, Giordano B, CKayser, Rousselet G, Gross J, Schyns P. A statistical framework for neuroimag-
592 ing data analysis based on mutual information estimated via a gaussian copula. *Hum. Brain Mapp.* **38**
593 (2017) 1541–1573.
594 [68] Wibral M, Pampu N, Priesemann V, Seiwert FSH, Lindner M, J T Lizier RV. Measuring information-
595 transfer delays. *PLoS One* **8** (2013) 2.
596 [69] Risken H. *The Fokker-Planck equation — Methods of solution and applications* (Berlin: Springer)
597 (1989).
598 [70] Arnold L. *Random Dynamical Systems* (Springer-Verlag, Berlin) (1998).
599 [71] Xu C, Roberts A. On the low-dimensional modelling of Stratonovich stochastic differential equations.
600 *Physica A* **225** (1996) 62–80.
601 [72] Derrida B, Gardner E, Zippelius A. An exactly solvable asymmetric neural network model.
602 *Europhys. Lett.* **4** (1987) 187.
603 [73] Touboul JD, Piette C, Venance L, Ermentrout G. Noise-induced synchronization and antiresonance in
604 interacting excitable systems: Applications to deep brain stimulation in parkinson's disease. *Phys. Rev.*
605 *X* **10** (2019) 011073. doi:10.1103/PhysRevX.10.011073.
606 [74] El Boustani S, Destexhe A. A master equation formalism for macroscopic modeling of asynchronous
607 irregular activity states. *neural Computation* **21** (2009) 46–100.
608 [75] Soula H, Chow C. Stochastic dynamics of a finite-size spiking neural network. *Neural Comput.* **19**
609 (2007) 3262–92. doi:10.1162/neco.2007.19.12.3262.
610 [76] Montbrio E, Pazo D, Roxin A. Macroscopic description for networks of spiking neurons. *Phys. Rev.*
611 *X* **5** (2015) 021028.
612 [77] Brunel N, Hakim V. Fast global oscillations in networks of integrate-and-fire neurons with low firing
613 rates. *Neural Comp.* **11** (1999) 1621–1671.
614 [78] Roxin A, Brunel N, Hansel D. Rate models with delays and the dynamics of large networks of spiking
615 models. *Prog. Theor. Phys.* **161** (2006) 68–85.
616 [79] Fourcaud N, Brunel N. Dynamics of the firing probability of noisy integrate-and-fire neurons. *Neural*
617 *Comput.* **14** (2002) 2057–2110.
618 [80] di Volo M, Torcini A. Transition from asynchronous to oscillatory dynamics in balanced spiking
619 networks with instantaneous synapses. *Phys. Rev. Lett.* **121** (2018) 128301.
620 [81] Arenas A, Díaz-Guilera A, Kurths J, Moreno Y, Zhou C. Synchronization in complex networks.
621 *Physics Reports* **469** (2008) 93–153. doi:https://doi.org/10.1016/j.physrep.2008.09.002.
622 [82] Della Rossa F, DeLellis P. Stochastic master stability function for noisy complex networks. *Phys, Rev. E*
623 **101** (2020) 052211.
624 [83] Hellwig B. A quantitative analysis of the local connectivity between pyramidal neurons in layers 2/3
625 of the rat visual cortex. *Biol.Cybern.* **82** (2000) 111–121.
626 [84] Yan G, Martinez N, Liu YY. Degree heterogeneity and stability of ecological networks. *J. R. Soc.*
627 *Interface* **14** (2017) 20170189. doi:10.1098/rsif.2017.0189.
628 [85] Hutt A, Buhry L. Study of GABAergic extra-synaptic tonic inhibition in single neurons and neural
629 populations by traversing neural scales: application to propofol-induced anaesthesia. *J. Comput.*
630 *Neurosci.* **37** (2014) 417–437.
631 [86] Brunel N. Dynamics of sparsely connected networks of excitatory and inhibitory spiking neurons. *J.*
632 *Comput. Neurosci.* **8** (2000) 183–208.

[87] Steinmetz P, Roy A, Fitzgerald P, Hsiao S, Johnson K, Niebur E. Attention modulates synchronized neuronal firing in primate somatosensory cortex. *Nature* **404** (2000) 187–190.

[88] Coull J. Neural correlates of attention and arousal: insights from electrophysiology, functional neuroimaging and psychopharmacology. *Prog. Neurobiol.* **55** (201998) 343–361. doi:10.1016/s0301-0082(98)00011-2.

[89] Lakatos P, Szilagyi N, Pincze Z, Rajkai C, Ulbert I, Karmos G. Attention and arousal related modulation of spontaneous gamma-activity in the auditory cortex of the cat. *Brain Res. Cogn. Brain Res.* **19** (2004) 1–9. doi:10.1016/j.cogbrainres.2003.10.023.

[90] Kinomura S, Larsson J, Gulyas B, Roland P. Activation by attention of the human reticular formation and thalamic intralaminar nuclei. *Science* **271** (1996) 512–515. doi:10.1126/science.271.5248.512.

[91] Galbraith G, Olfman D, Huffman T. Selective attention affects human brain stem frequency-following response. *Neuroreport* **14** (2003) 735–738. doi:10.1097/00001756-200304150-00015.

[92] Koval'zon V. Ascending reticular activating system of the brain. *Transl. Neurosci. Clin.* **2** (2016) 275–285. doi:10.18679/CN11-6030/R.2016.034.

[93] Serences J. Neural mechanisms of information storage in visual short-term memory. *Vision Research* **128** (2016) 53–67. doi:10.1016/j.visres.2016.09.010.